ultramicroscopy

A journal committed to the advancement of new methods, tools and theories in microscopy

http://www.elsevier.com/locate/ultramic

Available online at www.sciencedirect.com

ScienceDirect

Contents lists available at ScienceDirect

Ultramicroscopy

journal homepage: www.elsevier.com/locate/ultramic

Optimization of STEM tomography acquisition — A comparison of convergent beam and parallel beam STEM tomography

Johannes Biskupek *, Jens Leschner, Paul Walther, Ute Kaiser

Central Facility of Electron Microscopy, Ulm University, Albert-Einstein-Allee 11, D-89081 Ulm, Germany

ARTICLE INFO

ABSTRACT

In this paper two imaging modes in a state-of-the-art scanning transmission electron microscope (STEM) are compared: conventional STEM with a convergent beam (referred to as nanoprobe) and STEM with a parallel beam (referred to as microprobe). The effect and influence of both modes with respect to their depth of field are investigated. Tomograms of a human white blood cell (hemophagocytes) are acquired, aligned, and evaluated. It is shown that STEM using a parallel beam produces tomograms with fewer distortions and artifacts that allows resolving finer features. Microprobe STEM tomography is advantageous especially in life science, when semi-thin sections (approximately 0.5 μm thick) of biological samples are imaged at relatively low magnification with a large field of view.

1. Introduction

Electron tomography has been developed and improved during the past four decades [1] and has become a well established method. It was first applied and used predominantly in bright-field TEM mode with life science samples, where non-crystalline structures are present. Bright-field imaging of crystalline samples suffers from diffraction contrast, which does not fulfill the projection requirement and thus cannot be used for tomographic reconstruction. To overcome this limitation, Z-contrast imaging is a common option in scanning transmission electron microscopes (STEM) [2–4]. Z-contrast STEM tomography was first applied by Midgley et al. [5] and became state-of-the-art in materials science during the last decade. Moreover, it was shown by Yakushevska et al. [6] that Z-contrast STEM tomography of heavy metal stained life science samples is superior to bright-field TEM tomography providing better contrast and higher signal to noise ratio.

Nowadays, STEM tomography is used to obtain three-dimensional structural information with nanometer [7] to sub-nanometer resolution [8]. Z-contrast in STEM is realized by using an annular dark-field (ADF) detector collecting electrons scattered to high angles [5]. Fine probe sizes (down to sub-Å) and relative large semi-convergence angles (10 mrad in uncorrected STEM systems, 15 to 20 mrad in C_S corrected STEM systems) are usually used in STEM imaging. STEM also allows keeping the probe focused on a tilted sample by varying the strength of the probe-forming lens line by line during scanning [9]. Using this dynamic focus in STEM tomography supersedes the standard STEM and bright-field TEM tomography, especially if investigating larger specimen areas [10]. In practice, dynamic STEM focus is calibrated keeping the sample focused at three different heights for 0° tilt (usually eucentric height and offsets of ± 5 μm) [11]. For this approach it is assumed that the change of lens excitation scales linearly with focus. This approximation is valid within a focus range of about ± 5–10 μm [9,10]. However, also dynamic STEM focus has its limitations: focus is varied linearly with respect to sample height working correctly only for perfect slab-like samples. For bent, wedge-shaped or rod-shaped samples dynamic focus is not applicable and therefore conventional software automation routines fail. Very large focus variations (more than ± 10 μm, usually required for acquisition of tomograms with large field of view) result in magnification changes and distortions due to non-constant convergence angles and the influence of rotation center alignment. In addition, the simple approximation of a linear dependence between lens current (lens excitation) and focus change is not valid for larger changes of focus.

In optics, depth of field (DOF) is defined as thickness of the layer in which details appear sharp with the same resolution. Assuming an amorphous object and single scattering, the DOF is given by the well-known formula:

$$DOF \approx 2\frac{d^2}{\lambda}, \quad d = \frac{0.61\lambda}{\sin\alpha}$$

Here λ is the wavelength of the electron, d the resolution limit defined by the Raleigh criteria, and α is the semi-convergence angle.

* Corresponding author.
  E-mail address: Johannes.Biskupek@uni-ulm.de (J. Biskupek).

For conventional STEM this means that the small probe size comes at the expense of an equally small DOF (some tens of nm for uncorrected systems). The fine probe is usually focused on one surface of the sample and as a consequence of the small DOF, objects buried inside a thick sample or positioned at the opposite surface are out of focus and appear blurred. Conventional STEM tomography suffers from a loss in resolution when imaging thick specimens. However, scanning confocal electron microscopy (SCEM) benefits from narrow depth of field offered in corrected microscopes [12–14]. Three-dimensional information can be obtained by acquiring through-focal series of the sample [15]. However, SCEM requires a TEM with image and probe correctors, which have to be precisely tuned and aligned with respect to each other.

Thicker samples and samples containing a large amount of heavy elements lead to broadening of the probe because of multiple scattering [16,17]. Thus, information collected from the top of the sample originates from a smaller probe area than information collected from the bottom of the sample. The result is again a loss of resolution depending on sample thickness, sample density, setup of ADF detector, and initial convergence angle [18,19].

Both effects, beam broadening and small DOF, contribute to resolution and information loss in conventional STEM tomography. The DOF can be increased when the convergence angle is reduced. STEM tomography using an almost parallel beam should therefore suffer less from losses of resolution and information. The advantages of parallel STEM illumination and its possible applications for tomography were first evaluated and described in the works of Muller et al. [18] followed by others (e.g. [10,19–21]).

State-of-the art microscopes featuring three-condenser systems (e.g. FEI Titan 80-300 [21,22]) enable new imaging modes. A parallel beam with a small probe size (in the following referred to as "*microprobe*") can be formed, in contrast to the broad parallel beam in traditional TEM mode and the small convergent probe (in the following referred to as "*nanoprobe*") in traditional STEM mode.

In this paper we investigate the differences between conventional STEM tomography with a convergent beam (nanoprobe mode) and STEM tomography using a small parallel beam (microprobe mode) in terms of DOF, distortion, and artifacts within single images, and the influence of these features on aligned and reconstructed tomograms.

2. Materials and methods

Two basic samples have been investigated: standard gold cross-gratings and human white blood cells.

2.1. Standard gold cross-gratings

These are commercially available Au nanoparticles distributed over 463 nm sized squares on thin carbon films (e.g. Plano GmbH, Wetzlar, Germany, ordering number S106).

2.2. Human white blood cells

Human white blood cells (hemophagocytes) were cultivated on sapphire discs and high pressure frozen directly from the living state using a Compact-01 high pressure freezing machine (Wohlwend GmbH, Sennwald, Switzerland) and freeze substituted as described in [23]. Afterwards, samples were embedded in Epon. Semi-thin sections (0.5 μm) were cut on a Leica ultra

microtome E, mounted on special grids using poly lysine, exposed to a solution of 10 nm colloidal gold particles, serving as fiducial markers. Both sides were coated with thin (~5 nm) layers of carbon by electron beam evaporation.

2.3. Scanning transmission electron microscopy

STEM was carried out using a FEI 80-300 Titan Supertwin lens TEM operating at 300 kV equipped with a Fischione HAADF STEM detector and Fischione tomography holders (2020 advanced tomography holder and 2040 dual-axis tomography holder). As first mode, FEI's "nanoprobe" STEM offered by standard microscope alignment has been used. The microscope settings were: 3950 V extraction voltage, 650 V gun lens excitation, spotsize 9 (C1 lens excitation), semi-convergence angle of 10.0 mrad (weak excitation of C2 and C3 lenses) and a minimum excitation of the minicondensor lens. These settings allow to achieve a point-to-point STEM resolution of ~0.14 nm. The second mode, called "microprobe" was manually set up by using free lens control settings. The settings were: 3950 V extraction voltage, 1500 V gun lens excitation, smallest spotsize 11 (strongest possible C1 lens excitation), strong excitations of C2 and C3 lenses and a maximal excitation of the minicondensor lens. These settings allow the lowering of the semi-convergence angle down to 0.6 mrad (50 μm C2 aperture) in contrast to about 7 mrad, which is the smallest possible semi-convergence angle in conventional nanoprobe STEM (50 μm C2 aperture). The semi-convergence angle was measured on a thin TEM lamella of [1 1 0] orientated Si. These condensor settings result in a probe size of 2 nm. Fig. 1 shows the probe profile. The small Au particles of the cross-grating samples are nicely resolved, indicating a STEM resolution of about 2 nm. A comparison of the resolution between
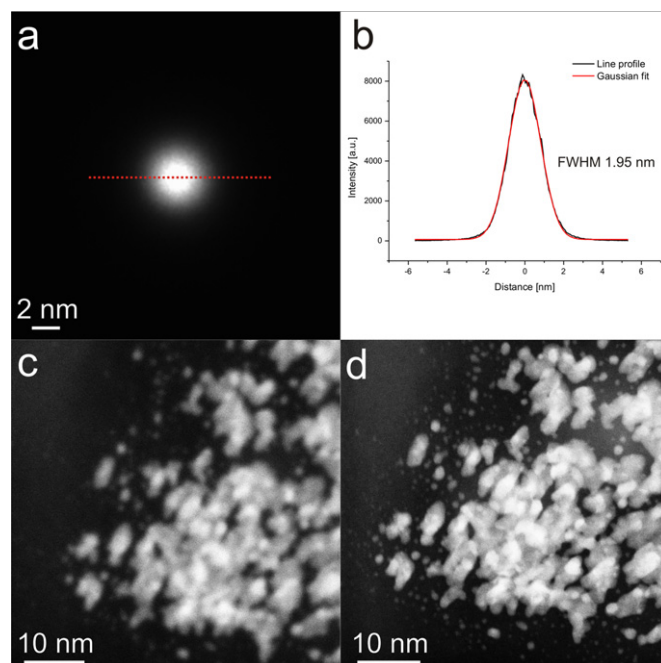

Fig. 1. Resolution of the microprobe mode. (a) Shows the image of the STEM probe using the microprobe mode. The dotted line indicates the direction of the line profile. (b) Shows a line profile of the curve (black) and fitted Gaussian (red). A full width half maximum (FWHM) of 1.95 nm was determined. (c) Presents a high magnification STEM image of small Au particles using microprobe mode. (d) Presents a high magnification STEM image of small Au particles using nanoprobe mode. Please compare the resolution between both modes. Microprobe mode is only sufficient to image structures with minimum sizes of about 2 nm and not suitable for high resolution imaging. (For interpretation of the references to color in this figure legend, the reader is referred to the web version of this article.)

microprobe and nanoprobe STEM mode is shown in Fig. 1c and d, respectively.

Tilt images and tomograms were acquired with dynamic focus enabled/disabled for nanoprobe and microprobe mode, respectively.

2.4. Tomogram acquisition, alignment and reconstruction

Tomograms were acquired using automatic routines (FEI software XPlore 3D) with a linear tilt scheme of 2° steps. Tomogram alignment was performed within the IMOD software package [24] by cross-correlation alignment followed by feature tracking using gold beads as fiducial markers. The same gold beads (25 in total) have been used as fiducials for both kinds of data sets (nanoprobe and microprobe tilt series). Tracking was continued in an iterative way until the mean residual of the pixel shifts (deviation between set position and theoretically predicted position) was better than 0.3 pixel and the standard deviation of the shifts was better than 0.2 pixel.

For reconstruction the SIRT algorithm of the Inspect 3D (FEI company) tomography software was used with 25 iterations.

3. Results and discussion

3.1. Limits of dynamic focus and depth of field of nanoprobe and microprobe STEM — Calibration sample

Fig. 2 shows STEM images of gold cross-gratings recorded at 70° tilt, either applying nanoprobe STEM mode with constant focus (Fig. 1a) and with dynamic focus (Fig. 2b), or microprobe STEM mode (Fig. 2c) studying DOF with respect to each mode. A dual-axis holder was used to compensate rotation between different STEM modes. Using constant focus nanoprobe STEM an area of only approximately 3 μm to each side of the tilt axis is in focus. Applying dynamic focus has a beneficial impact (Fig. 2b), but objects along the edges parallel to the tilt axis are still completely out of focus. Using microprobe STEM (Fig. 2c), however, results in better focused images than both nanoprobe modes, as all features of the images are clearly resolved, indicating a large DOF.

In Fig. 3 the DOF of nanoprobe and microprobe STEM is further exemplified by moving an Au cross-grating off eucentric stage height (relative $z=0$ μm). Varying stage height by ± 15 μm shows no degradation of focus quality and only a slight image rotation of 0.4° for microprobe mode; while for nanoprobe the image is almost completely out of focus. A larger change of z-position (± 30 μm) leads to noticeable rotation of the image for

microprobe mode by about 2.0° due to spiraling motion of electrons along the optical axis. The 463 nm wide squares and the surface features are still kept relatively well in focus. However, for the same z-shift nanoprobe mode results in completely unfocused images that are inadequate for data evaluation. The large depth of field makes microprobe an ideal mode for acquisition of tomograms.

3.2. Analysis of microprobe and nanoprobe STEM tomography — Biological sample

Fig. 4 shows nanoprobe and microprobe STEM tilt series' images (tilt range ± 72°, 2° tilt increment) of a 0.5 μm thick section of the peripheral area of a human white blood cell (hemophagocyte) for assessment of mode-dependent imaging quality. For comparison of both modes the same sample area has been taken into account; however, the field of view differs slightly by ~ 5%. We attribute this to different excitations of condensor settings resulting in a change of effective magnification. Choosing 20,000 times magnification the image pixel size was 2.8 and 2.9 nm/pixel for nanoprobe and microprobe, respectively. The naked eye inspection shows a similar image quality for both center regions. The difference in image quality is assessed in more details by investigating the shape of small features such as the gold beads. The microprobe STEM images (Fig. 4d–f) show finely resolved gold beads over the whole image area, even at high tilt. In contrast, nanoprobe STEM images show the gold beads blurred in top and bottom areas (Fig. 4a and c, compare also the magnified images Fig. 4g–j). Quantitatively, this can be determined by estimating the point-spread-function by full width at half maximum (FWHM) measurement of differently blurred gold beads (Fig. 5). Here, the left bottom part of Fig. 4c and f are magnified and two exemplary gold beads are encircled. The plots in Fig. 5 show linescans across the encircled gold beads (directions of linescans are always horizontal) and the resulting Gaussian fit for FWHM estimation. The FHWM of gold beads in microprobe images is much smaller than in nanoprobe images. Especially, gold bead #2, close to the bottom edge of the image, shows a FWHM of 6.2 nm in microprobe (Fig. 5e), compared to 18.4 nm in nanoprobe mode (Fig. 5c)—a threefold increase. The effect is less pronounced for gold bead #1, which is closer to the center of the image and therefore closer to the tilt axis.

The alignment process, which is crucial for three-dimensional reconstruction (cf. next paragraph), provides statistical measures to assess differences in both microprobe and nanoprobe modes for tilted specimens. These measures are accessible by the IMOD package within the log file of the feature tracking alignment process for which the gold beads have been used as fiducials.
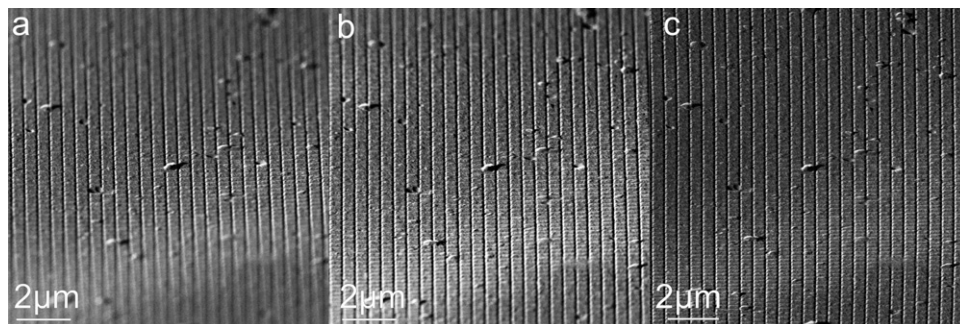

Fig. 2. STEM images of Au cross-gratings recorded at 70° stage tilt and various imaging modes (tilt axis is horizontally in the middle). A dual axis tomography holder was used to align the direction of squares for each mode. (a) Is imaged with standard nanoprobe STEM mode with constant focus (dynamic focus was disabled). The limited depth of field lowers the resolution of objects far away from eucentric height. (b) Is recorded with nanoprobe STEM together with dynamic focus. (c) Is recorded with microprobe mode. Only in (c) most of the features (fine squares and defects within) are well in focus. Please note that bending of the foil leads to additional blurring of features in (a) and (b) but not in (c).
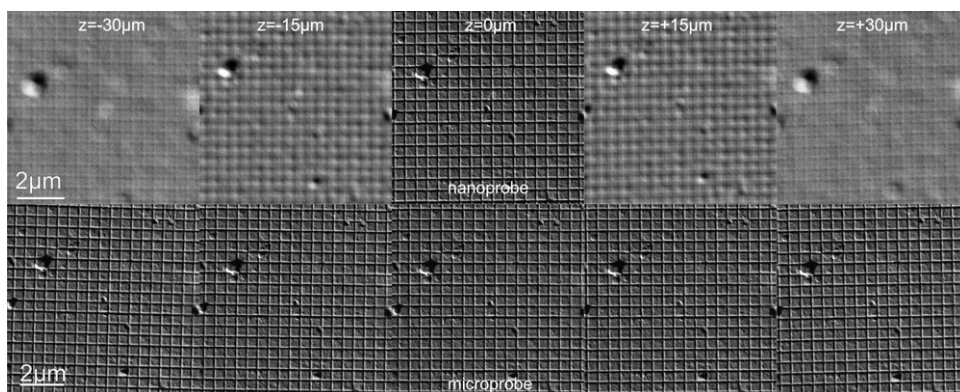
Fig. 3. Depth of field of nanoprobe and microprobe STEM imaging. STEM images of an Au cross grating acquired using nanoprobe (upper row) and microprobe (lower row) at constant focus but different sample z-height are shown. A change of z by $\pm 15\,\mu m$ produces highly unfocussed images for the case of nanoprobe; $\pm 30\,\mu m$ produces inadequate images. For the case of microprobe, a change of z by $\pm 15\,\mu m$ leads to small image rotation of $0.4°$ to the right or to the left, respectively, a higher change of z by $30\,\mu m$ to a larger image rotation of $2.0°$. However, all images appear sharp and focused independent of the large change of z-height.
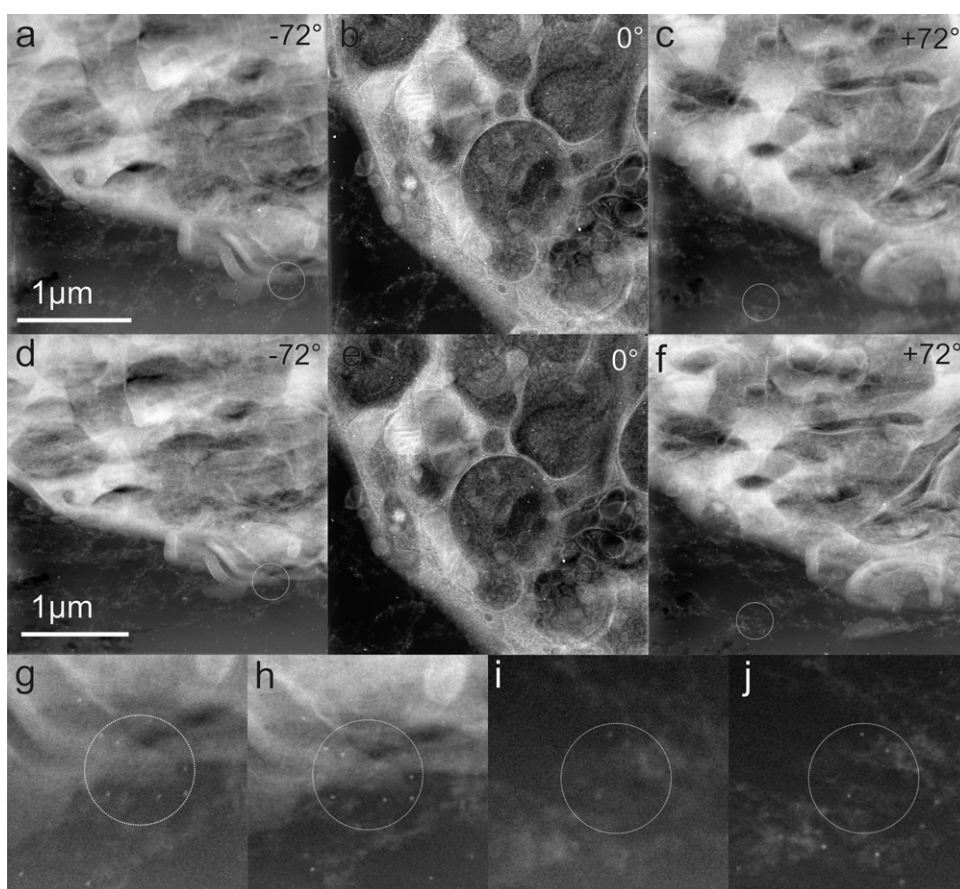

Fig. 4. Comparison of nanoprobe STEM (a)–(c) and microprobe STEM (d)–(f) tilt images. The same area and about the same field of view of a white blood cell are shown in both imaging modes. The high tilt images of microprobe STEM images (d) and (f) show higher contrast and sharper features at top and bottom areas than the corresponding nanoprobe STEM images (a) and (c). Please compare and notice the differences of the encircled areas that mark some exemplary gold beads; (g) and (h) show enlarged areas of the encircled gold beads in (a), (d) while (i), (j) show enlarged areas of the encircled beads in (c), (f).

Most interesting are the changes of magnification (internally called by IMOD "*demag*") and the tilt angle corrections for the actual image (internally called by IMOD "*deltilt*"). *Demag* and *deltilt* are stretch variables that are strongly influenced by magnification changes and image rotation because of strong under- and over focus (present in dynamic focus at high tilt) and rotation center alignment (not constant when focus is varied over larger scale). Thus, the necessary corrections for the case of microprobe STEM are much smaller than for nanoprobe

STEM, especially at high tilt, illustrating a more perfect imaging process across the field of view (Fig. 6). Nevertheless, the estimated corrections led to equally well aligned microprobe and nanoprobe tilt series allowing comparable three-dimensional reconstructions.

Slices of a boundary region of the reconstructed 3D volume of both the nanoprobe (Fig. 7a) and microprobe (Fig. 7b) data set are depicted in Fig. 7. Please note that there is a small shift between both reconstructions due to the offset in the field of view; the
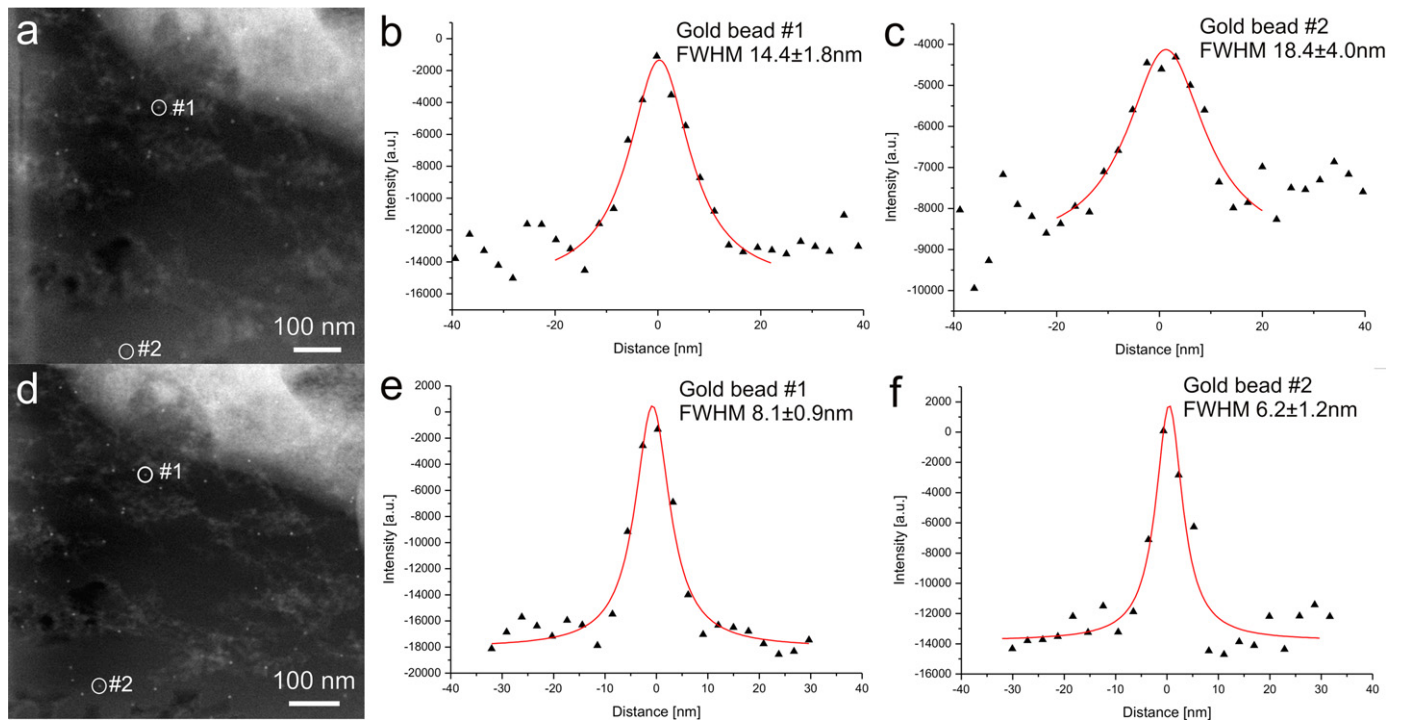
Fig. 5. (a) and (d) show enlarged areas of the bottom left regions presented earlier in Fig. 3c and f: (a) shows the nanoprobe tilt image while (d) shows the microprobe tilt image (both at 72°). Corresponding gold beads are encircled in both images. It can be clearly seen that the gold beads in (a) are more blurred than in (d). The graphs (b), (c), (e), and (f) show plots of horizontal linescans along gold beads #1 and #2. The FWHM was determined by fitting Gaussian peaks. The FHWM of gold beads of nanoprobe images (b) and (c) are much larger than that of microprobe images (e) and (f).
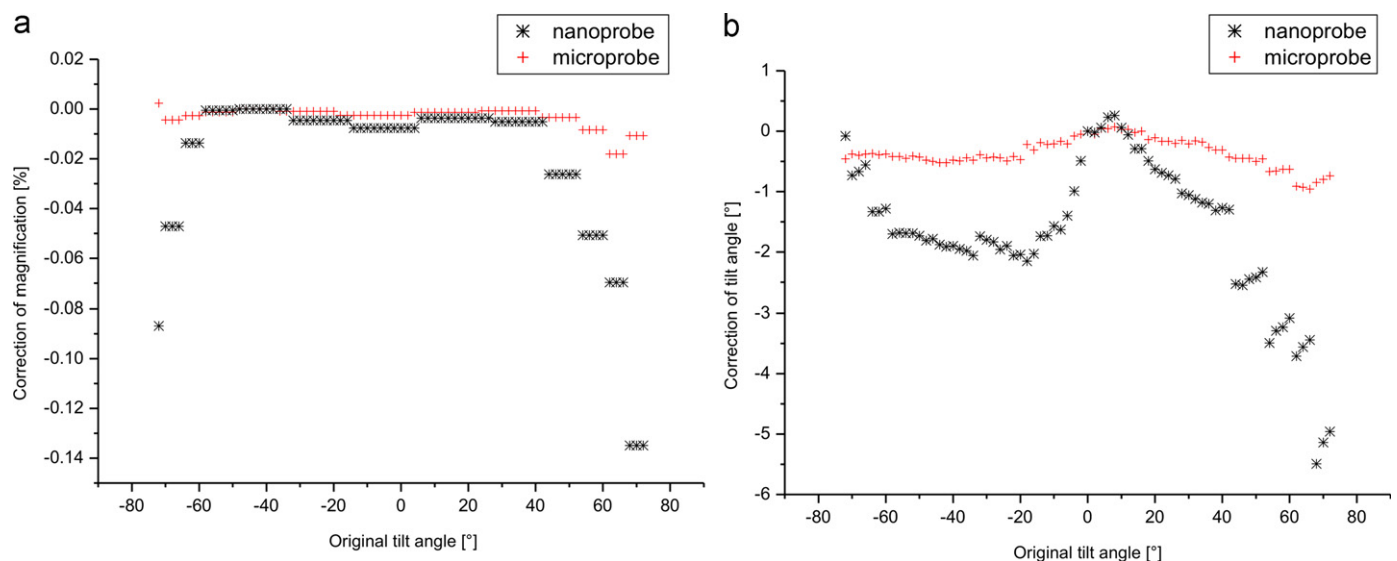

Fig. 6. The plots show the applied corrections onto the acquired tilt images by IMOD for microprobe and nanoprobe STEM data: (a) shows the change of magnification and (b) shows the correction of tilt angles. Both corrections required for microprobe data are much smaller than for nanoprobe data.

corresponding object areas are marked by dotted cross-hairs. A better contrast in the microprobe slice (Fig. 7b) and remarkably less blurring of features in y- and z-slices can be seen by the naked eye as the main difference between the two SIRT reconstructions. Whereas the missing wedge artifact is prevalent in both series due to identical tilt parameters for acquisition, the streaking is less intense for the microprobe data. Blurring in the 3D volume results from blurring during acquisition, alignment imperfections, and reconstruction artifacts. Image intensities and tilt parameters are identical in both series and alignment was carried out to the accuracy limit, and visually checked afterwards (inspection of the

trajectories of gold beads after alignment). We can conclude that the gain in contrast is caused by reduced blurring in microprobe mode and we also have to point out that this is not an effect of "tuning" or "optimizing" contrast, brightness and gamma function. All images shown in Fig. 7 (same case for images in Fig. 8 presented later in the text) have exactly the same conditions for visualization: displayed grey value 0 in the figures corresponds to minimum grey value of the original 16 bit signed grey scale data; displayed grey value 255 corresponds to the largest grey scale data; we used a gamma value of 2.2 (Adobe sRGB color space) and a linear scaling of contrast and brightness.
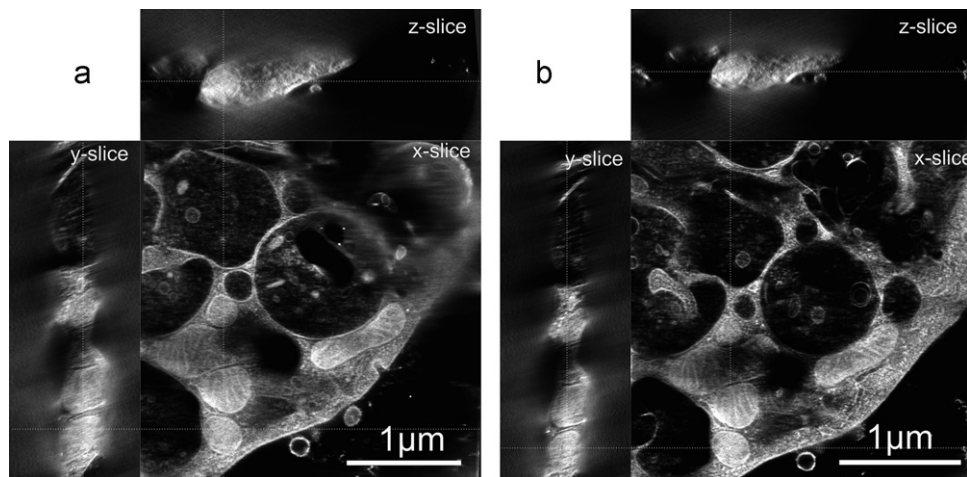
Fig. 7. x-, y-, z-slices of SIRT reconstructed nanoprobe (a) and microprobe (b) data sets (the dotted cross-hair marks the intersection of slice projections).
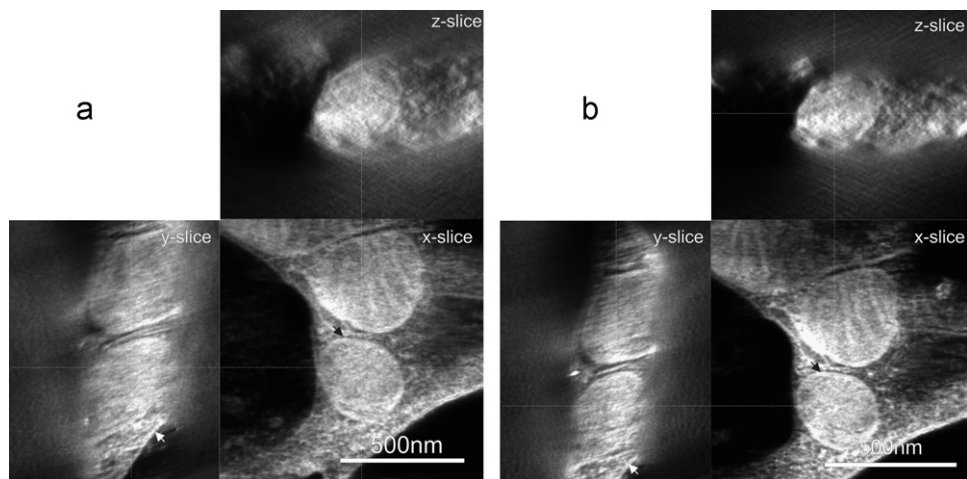

Fig. 8. Magnified slices of nanoprobe (a) and microprobe (b) volumes (the dotted cross-hair marks the intersection of slice projections). The black arrow depicts the mitochondrial membranes. The two bi-layers are better visible in microprobe. The white arrow depicts the plasma membrane, which is clearer visible in microprobe than in nanoprobe.

For better illustration Fig. 8 shows magnified details of the slices presented in Fig. 7. The black arrow depicts the mitochondrial membranes. The two bi-layers are better visible in microprobe. The white arrow depicts the plasma membrane, which is clearer visible in microprobe than in nanoprobe.

contrast of slices in the reconstructed 3D volumes, especially at the boundaries of the reconstructed volume. It can be concluded that the proposed microprobe mode results in an improvement in acquisition techniques for tomograms requiring a large field of view for semi-thin sections of life science specimen.

4. Conclusion

We have compared standard convergent beam (nanoprobe) STEM with parallel beam (microprobe) STEM. Microprobe has been shown to posses a larger depth of field (up to $\pm 30\,\mu m$), thus, all features are kept in focus even at large tilt without the necessity to apply specimen topography-dependent dynamic focus. A decrease of measured FWHM of gold beads at high tilt, by a factor of three, shows a gain in resolution by microprobe. Thus, for the case of thick specimens and almost parallel beam shape (convergence angle ~ 20 times smaller than for convergent nanoprobe beam) resolution is only limited by beam broadening caused by scattering. Tilt series alignment data shows that at high tilt fewer corrections (magnification and tilt angle correction) are necessary in the case of microprobe data, thus, ensuring better imaging quality over the entire field of view. Less blurring in the 2D images of a microprobe tilt-series resulted in much better

References

[1] R.A. Crowther, D.J. DeRosier, A. Klug, The reconstruction of a three-dimensional structure from its projections and its application to electron microscopy, Proc. R. Soc. Lond. (A) 317 (1970) 319–340.
[2] A.V. Crewe, J. Wall, J. Langmore, Visibility of single atoms, Science 168 (1970) 1338–1340.
[3] M.M. Tracy, A. Howie, C.J. Wilson, Z-contrast of platinum and paladium catalysts, Philos. Mag. A 38 (1979) 569–585.

[4] A. Howie, Image contrast and localized signal selection techniques, J. Microsc. 17 (1979) 11–23.

[5] P.A. Midgley, M. Weyland, J.M. Thomas, B.F.G. Johnson, Z-contrast tomography: a technique in 3-dimensional nanostructural analysis based on Rutherford scattering, Chem. Commun. 18 (2001) 907–908.

[6] A.E. Yakushevska, M.N. Lebbink, W.J. Geerts, L. Spek, E.G. van Donselaar, K.A. Jansen, B.M. Humbel, J.A. Post, A.J. Verkleij, A.J. Koster, STEM tomography in cell biology, J. Struct. Biol. 159 (2007) 381–391.

[7] I. Arslan, T.J.V. Yates, N.D. Browning, P.A. Midgley, Embedded nanostructures revealed in three dimensions, Science 309 (2005) 2195–2198.

[8] D.A. Muller, J. Grazul, Optimizing the environment for sub-0.2 nm scanning transmission electron microscopy, J. Electron. Microsc. 50 (2001) 219–226.

[9] C. Kübel, A. Voigt, R. Schoenmakers, M. Otten, S. David, T.C. Lee, A. Carlsson, J. Bradley, Recent advances in electron tomography: TEM and HAADF-STEM, tomography for materials science and semiconductor applications, Microsc. Microanal. 11 (2005) 378–400.

[10] K. Aoyama, T. Takagi, A. Hirase, A. Miyazawa, STEM tomography for thick biological specimens, Ultramicroscopy 109 (2008) 70–80.

[11] A. Voigt, C. Kübel, FEI XPlore 3D Step-by-Step Guide, FEI Company, 2005.

[12] N.J. Zaluzec, The scanning confocal electron microscope, Microsc. Today 6 (2006) 8.

[13] E.C. Cosgriff, A.J. D'Alfonso, L.J. Allen, S.D. Findlay, A.I. Kirkland, P.D. Nellist, Three-dimensional imaging in double aberration-corrected scanning confocal electron microscopy, Part I: elastic scattering, Ultramicroscopy 108 (2008) 1558–1566.

[14] A.J. D'Alfonso, E.C. Cosgriff, S.D. Findlay, G. Behan, A.I. Kirkland, P.D. Nellist, L.J. Allen, Three-dimensional imaging in double aberration-corrected scanning confocal electron microscopy, Part II: inelastic scattering, Ultramicroscopy 108 (2008) 1567–1578.

[15] G. Behan, P.D. Nellist, Optical depth sectioning in the aberration-corrected scanning transmission and scanning confocal electron microscope, J. Phys. 126 (2008) 012083.

[16] D.J. Smith, J.M. Cowley, Aperture contrast in thick amorphous specimens using scanning transmission electron microscopy, Ultramicroscopy 1 (1975) 127–136.

[17] H. Rose, J. Fertig, Influence of detector geometry on image properties of the stem for thick objects, Ultramicroscopy 2 (1976-1977) 77–87.

[18] J.K. Hyun, P. Ercius, D.A. Muller, Beam spreading and spatial resolution in thick organic specimens, Ultramicroscopy 109 (2008) 1–7.

[19] A.A. Sousa, M.F. Hohmann-Marriott, G. Zhang, R.D. Leapman, Monte Carlo electron-trajectory simulations in bright-field and dark-field STEM: implications for tomography of thick biological sections, Ultramicroscopy 109 (2009) 213–221.

[20] M.F. Hohmann-Marriott, A.A. Sousa, A.A. Azari, S. Glushakova, G. Zhang, J. Zimmerberg, J.R.D. Leapman, Nanoscale 3D cellular imaging by axial scanning transmission electron tomography, Nat. Methods 6 (10) (2009) 729–731.

[21] J. Loos, E. Sourty, K. Lu, B. Freitag, D. Tang, D. Wall, Electron tomography on micrometer-thick specimens with nanometer resolution, Nano Lett. 9 (2009) 1704–1708.

[22] B. Freitag, R. Erni, K. Inoke, M. Stekelenburg, D. Hubert, Recent advances in aberration corrected TEM/STEM for materials research aberration corrected microscopy with newly developed platform, Microscopy 41 (2006) 21–25.

[23] C. Buser, P. Walther, Freeze-substitution: the addition of water to polar solvents enhances the retention of structure and acts at temperatures around −60 °C, J. Mircrosc. 230 (2008) 268–277.

[24] D.N. Mastronarde, Correction for non-perpendicularity of beam and tilt axis in tomographic reconstructions with the IMOD package, J. Microsc. 230 (2008) 212–215.